

## Chapter 2

# Instrument, Observations and Analysis Procedures

This chapter presents the details of the instrument and observations that were used for our study presented in this thesis. The telescope, our data acquisition system and analysis strategies are described. The main aim of our observations was to study pulsars for their average and single-pulse properties. Observations were made using the low frequency array at Gauribidanur (GEETEE), which are central to the theme of this thesis.

### 2.1 The Gauribidanur Telescope

The radio telescope at Gauribidanur (80 km North of Bangalore, India; latitude,  $13^{\circ}36'12''$ , longitude,  $77^{\circ}26'07''$ ) is a 'T'-shaped array (Figure 2.1) of 1000 broad-band fat dipoles, each  $\frac{3}{4}\lambda$  ( $\lambda=8.7$  m) long (Deshpande, Shevgaonkar, & Shastri, 1989).

#### 2.1.1 Parameters

The dipoles are oriented East-West (EW) and are sensitive to a 10-MHz band centered at 32 MHz. The EW arm is 1.38 km long, from the center of which a 0.45 km long arm extends southwards, giving a 'T'-shaped aperture (figure 2.2). The EW arm consists of 640 dipoles arranged in four rows of 160 dipoles each. Each row is separated by 5 m in the North-South (NS) direction. The total half-power beamwidth (HPBW) of the EW arm is  $21'$  and  $25^{\circ} \sec(Z)$ , in hour angle (HA) and declination respectively, at  $\lambda = 8.7$  m (where  $Z$  is the zenith angle). The south arm consists of 360 dipoles arranged in 90 rows and has total power beam widths of  $14.5''$  and  $69' \sec(Z)$  in HA and declination respectively.

The EW arm consists of 10 groups, each consisting of 64 dipoles combined in a Christmas-tree configuration, first along E-W and then along N-S. The outputs from the five groups each in



**Figure 2.1:** Low Frequency Array at Gauribidanur, India (GEETEE): the West-arm as viewed from the center of the T-array.

the east and the west are combined separately with equal amplification, and brought to the receiver room through equal-length radio-frequency (RF) cables. Amplifiers in the signal path compensate for the cable losses, and have a bandwidth of operation about 2 MHz. The EW arm has an effective area of about  $12000 \text{ m}^2$  at the instrumental zenith ( $+14^\circ.1$  declination). The telescope is essentially a meridian-transit instrument with only a limited tracking capability. The telescope can be electronically steered to any declination ( $\delta$ ) in the range from  $-45^\circ$  to  $75^\circ$  in steps of  $0.1^\circ$  and any source in this declination range can be tracked for a duration of  $42 \times \sec(\delta)$  min about the transit time.

### 2.1.2 Observation modes

The telescope can be used either in the correlation mode  $[(E \times W), \text{ or } (E + W) \times S]$ , or in the total power mode  $[(E + W)^2 \text{ or } (E + W + S)^2]$  (Deshpande, Shevgaonkar, Shastry, 1987). We used only the E W antenna in the total power mode for our observations, i.e.  $(E+W)^2$ . We used an available continuum receiver to monitor our observations. As the output of the receiver could be displayed either on a chart recorder or a computer screen with an appropriate interface, it was used for equalizing the phases of the E and W arms from visual inspection of the power pattern of the antenna, traced by the motion of a point source through the beam, It was also used to monitor the antenna performance during its test observations and as an interference monitor during our regular pulsar observations.

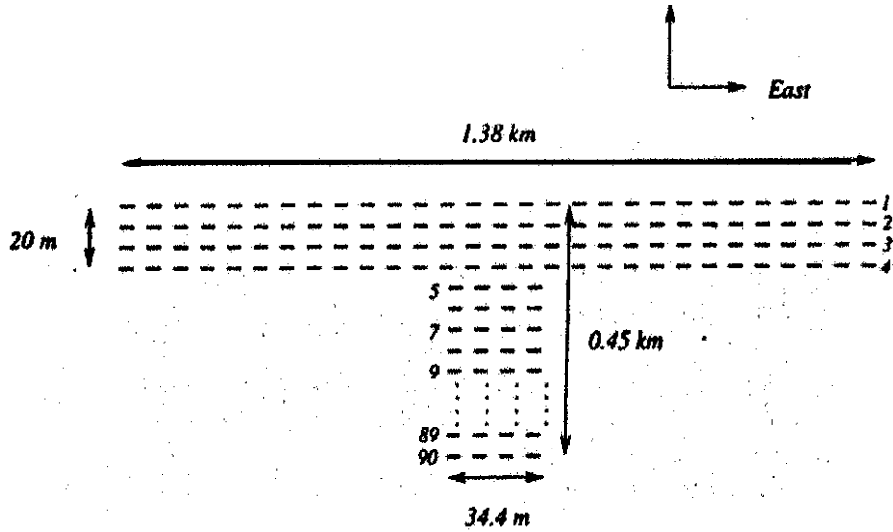


Figure 2.2: A schematic of the GEETEE (see text for details).

Any source within the declination range of GEETEE can be tracked between  $\pm 5^\circ$  in hour angle around the instrumental meridian. The maximum duration of tracking is  $40 \sec(\delta)$  min. Tracking in this angle of  $10^\circ$  is carried out in 63 tracking steps, where the beam of the telescope flips from one position to the next after each 'beam-flip time' of  $40 \sec(\delta)$  sec. The on-source response of the telescope, thus, is modulated over the time-scale of a beam-flip time due to systematic changes in the system gain.

A given part of the sky can also be monitored in the transit-mode, where the antenna points in a given direction. The voltages at the output of the antenna are recorded as the sky sources transit over the beam of the antenna. In our case, using the (E+W) total-power mode, a celestial source will require  $\sim 90$  seconds to transit over the half-power beam.

## 2.2 Back-end and data acquisition system

In a conventional approach, pulsar observing set-up involves a dedicated instrument to carry out a dedispersion scheme online. In such a scheme, the instrument is designed for observations using a pre-decided band of frequencies around a given central frequency. Such an 'online' dedispersion has several limitations as discussed in section 1.3.1.

We now describe our general purpose data-acquisition system (hereafter, DAS), which was built to be an independent unit that can be used in any observatory irrespective of certain details of the front-end receivers or bank-end instruments (Ramkumar, 1998, & Deshpande, Ramkumar,

|                                 |                             |
|---------------------------------|-----------------------------|
| Antenna latitude and longitude  | 13°36'12" N and 77°26'07" E |
| Instrumental zenith             | 14°.1 N                     |
| Declination coverage            | -46° to +74°                |
| Central Frequency and bandwidth | 34.5 MHz and 1-MHz          |
| Collecting area                 | 12,000 m <sup>2</sup>       |
| Antenna beam                    | 21' × 25° (RA × $\delta$ )  |
| On-source tracking possible     | 42 x sec( $\delta$ ) min    |
| Polarization                    | E-W                         |
| Observation mode                | (E+W) total-power           |

Table 2.1: Relevant parameters of our telescope as used in our observations.

Chandrasekaran, 2001). This unit can be used at the intermediate frequency (IF) end of any receiver system with bandwidths of a couple of megahertz. We digitize the incoming antenna voltages in a 2-bit, 4-level scheme, and sample them at Nyquist rate. The sampled raw voltages are stored on a PC disk directly and the suitably backed-up data are later analysed entirely in software. A schematic of this system is shown in figure 2.3. We now discuss various sections of this DAS.

### 2.2.1 Antenna output and RF section

Antenna output, *i.e.* (E + W) sum voltage signal at 34.5 MHz, was fed to the DAS. The DAS consists of three parts. Please refer to figure 2.3 for the block diagram of the DAS. The first one is the "Digitizer Unit" which digitalizes the input signal (IF) to three levels. The digitized information is fed to the second stage which is the "Bit-Packing Logic Unit". This unit converts the 2-bit data

into the 16-bit parallel information that is compatible with a PC data bus. The 16-bit data are provided to the "DAS PC ADD-ON" card, which interfaces with the PC. These three units are explained in detail in the following paragraphs.

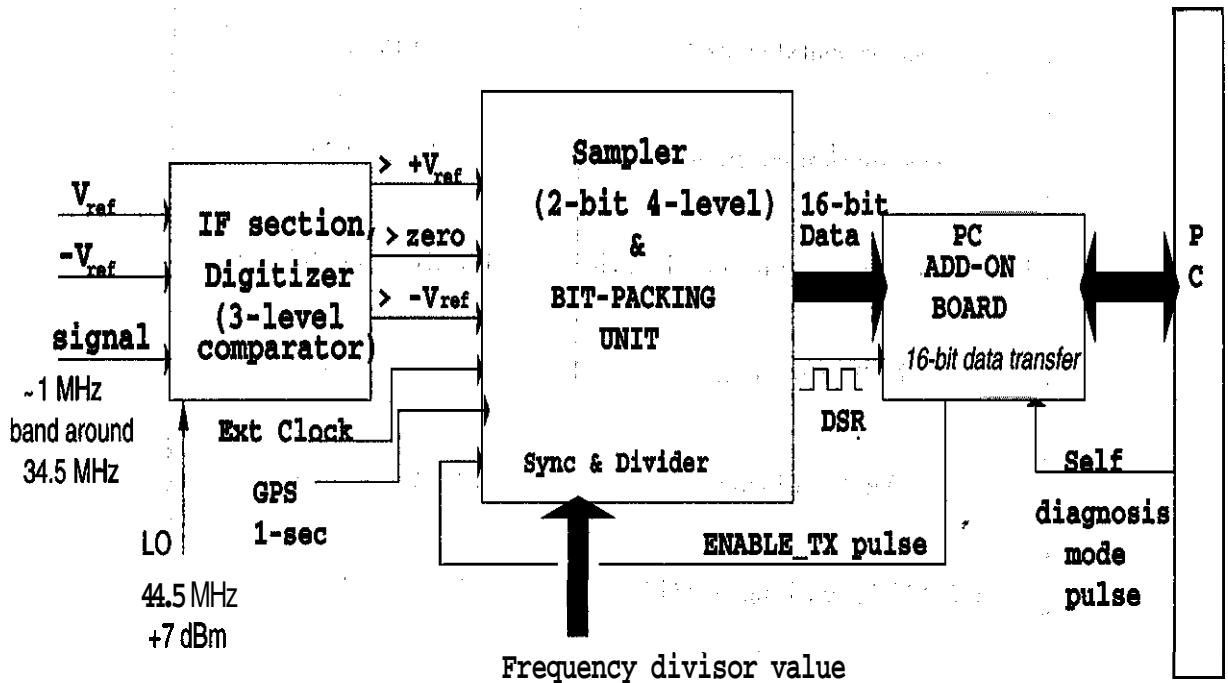


Figure 2.3: A schematic block diagram of the General Purpose Data Acquisition System (DAS). There are three main blocks, the Digitizer, Sampler and Bit-packing logic, and the PC Add-on Card. The Add-on card is interfaced with the PC. The entire data acquisition is controlled by an acquisition program on the PC.

### 2.2.2 Digitizer : IF section

The antenna signal at 34.5 MHz, with a bandwidth of  $\sim 2$  MHz after an adequate amplification, is down-converted to an IF of 10 MHz using a local oscillator (LO) frequency of 44.5 MHz at a power level of +7 dBm. After an appropriate amplification, we filter this signal to obtain a 3 dB bandwidth of 1-MHz around the central frequency of 10 MHz.

This unit further consists of three comparators which are realized using high-speed operational amplifiers (NE521). The input signal is ac-coupled to avoid any dc signal. This input signal level is compared to three reference voltage levels, a positive " $+V_{ref}$ ", a negative ref " $-V_{ref}$ ", and "Zero" level. Both  $+V_{ref}$  and  $-V_{ref}$  are generated from the same source, so that a deviation in  $+V_{ref}$  will be tracked by deviations in the  $-V_{ref}$ . Thus this unit generates three bits of information (TTL logic levels) which tells the statistics and the nature of the input signal. These bits are transferred on differential lines to the bit-packing logic unit.

### 2.2.3 Sampler and bit-packing

All the units needed for the bit-packing logic are realized in an 'Erasable Programmable Logic Device' (EPLD) chip (from Altera). To accommodate for any future changes in the logic only 70% to 80% of the logic cells of the EPLD are used.

A standard oscillator (of frequency  $f_s^{2n}$ ) is used as an input clock for this block. The data acquisition can be synchronized with a 1-second pulse from the Global Position System (GPS), if so desired. It is also gated with the "ENABLE-TX" pulse from the DAS PC ADD-ON board which indicates that the board is ready to accept data from the system. In order to facilitate the user to have a selectable sampling clock frequency, a divider logic is employed, which supports a division of the incoming frequency ( $f_s^{2n}$ ) up to a factor of 99. The user can select this divisor value through the front panel thumb wheel.

#### Harmonic sampling

In all our observations, we used  $f_s^{2n} = 21$  MHz, and a division factor of 10, which generates a sampling frequency ( $f_s$ ) of 2.1 MHz. The fifth harmonic of this frequency falls at 10.5 MHz. This mode of sampling is called Harmonic Sampling. It folds, among other bands, the band from 8.4 MHz to 10.5 MHz to a baseband from 0 to 2.1 MHz. We thus sample our signal band between 9.45 MHz and 10.5 MHz, where the band is flipped to fall between 0 to 1.05 MHz. This method allows us to sample a band located at a higher frequency with a low frequency sampler performing an implicit down-conversion, a definite advantage from the design point of view.

#### 3-bit comparator output to 2-bit sample conversion

A hardware for conversion from 3-bit comparator outputs to a 2-bit sample representation is realized using combination logic. Please refer to Table 2.2 for this conversion. This block is also incorporated in the EPLD in order to support any other conversion/coding, if needed at a future date. Thus, for every cycle of the sampling clock we will get a 2-bit data sample.

It is helpful to pack a suitable number of these 2-bit samples into a 16-bit word so that data transfer to the PC can be optimized, since the IESA bus used on a PC/AT supports a 16-bit data transfer. This, along with a more efficient storage of data onto the PC, necessitates the bit-packing logic. This block accepts two bits for each sampling clock and packs eight successive samples to a 16-bit word. Before these bits are passed to the PC bus, they can be multiplexed with another 16-bit word of locally generated "marker" data. Such a marker word has its eight most significant bits (MSB) as zeroes, with the least significant byte (LSB) acting as counter. For every 4K-words of

| Input from the comparator |              |       | Sampler Output |     | Signal Status               |
|---------------------------|--------------|-------|----------------|-----|-----------------------------|
| $< -V_{ref}$              | $> +V_{ref}$ | $> 0$ | MSB            | LSB | $V_{signal}$                |
| 0                         | 0            | 0     | 0              | 0   | $V_{signal} < -V_{ref}$     |
| 1                         | 0            | 0     | 0              | 1   | $-V_{ref} < V_{signal} < 0$ |
| 1                         | 0            | 1     | 1              | 0   | $0 < V_{signal} < +V_{ref}$ |
| 1                         | 1            | 1     | 1              | 1   | $V_{signal} > +V_{ref}$     |

Table 2.2: Table describing the conversion from a 3-bit comparator output to a **2-bit** 4-level sample.

actual data one such "marker" is inserted and the LSB counter is incremented. The LSB counter, thus keeps count (modulo 256) of the 4K-word blocks of data transferred. These counts are later used in checking for possible slips in the data acquisition.

#### 2.2.4 PC interface card

This card functions as an interface between the high-speed data acquisition system and a PC. It is provided with two data storage buffers, which are First-In First-Out (FIFO) memory devices. The data are written in FIFO, and are accessed by the acquisition program.

The real constraints on the data-acquisition rate come from the disk access time of a PC, and the FIFO memory size. Since data rates of the order of 0.5 MB per second are expected, the disk access time should be  $\lesssim 10\text{ms}$  for a FIFO of 8K. In the case of the disk access time being larger occasionally, it led to data slips in transfer. Such a loss in data can be checked using the markers mentioned above. We discuss this in the section on data analysis. In our later set-up, which was used for the present observations, a new PC was used with a much faster disk, and a larger FIFO (32K) on the PC ADD-ON card.

#### 2.2.5 Diagnostic mode

A self-diagnosis mode is incorporated to check the transmission of data from the EPLD to the PC bus. In this "diagnostics" mode of operation, bit-backing the EPLD acts as a pair of 8-bit counters and the count is decremented/incremented by appropriate signals from bit-packing logic. The counters are designed such that one of the two 8-bit counters counts in "up" and the other in

the "down" modes. This will write lower bytes in the ascending order and the upper bytes in the descending order. This pattern can be checked at the data file. Any deviations can then be traced in the hardware.

## **2.3 Off-line processing**

### **2.3.1 Data slip-check**

As mentioned in section 2.2.3, for every 4096 words of data, we insert a 16-bit marker. The most significant bits (**MSBs**) are zero, and the least significant bits (**LSBs**) are used as a counter from zero to 255. The general probability that a data would mimic such a behavior is small ( $\leq 1$  part in  $2^{16}$ ), and that for such a data to arrive at the expected successive locations of markers is negligible. An up counter (with **LSBs**) is incremented after every 4096 words. In the event of data loss, the missing number of markers as well as the data words found between the recovered markers would identify and quantify such a data loss. Once a loss of marker from its expected location was encountered, the next marker is identified by looking for a subsequent word which has its MS Byte equal to zero. Wherever a match occurred we read out the LSB of this word to check if a "sensible" value was found. From this marker onwards later markers will be traced for data loss as described above.

We note separately a copy of the first block of 4096 words of each data file when we begin the slip-check. Once we identify a missing block of data, we fill the "gap" with a pseudo-sequence obtained by randomizing the samples from the "noted 1<sup>st</sup> block". It should be noted that such data loss was almost never encountered in our observations.

### **2.3.2 Digitizer-level weight ages**

In the scheme of acquisition, the incoming signal voltages are sampled after digitization. Digital sampling is inherently a non-linear process: with a finite number of bits, 'quantization' noise will inevitably be added to the signal. The extreme case of 1-bit sampling, in which 'on' and 'off' values are assigned by comparing each sample to signal mean, yields the noisiest representation of the signal. The quantization we have chosen for DAS (**2-bit, 4-level**) is a significant improvement on 1-bit sampling, but still quite coarse. It was a compromise from the design point of view: the motivation was to keep the data rate and data sizes to a manageable level while sampling with more than one bit. The coarse quantization will necessarily affect the observed pulse shapes and signal-to-noise ratios, but in statistically predictable ways.

The primary concern in a coarsely quantized system is that of linearity, or in other words,



the dynamic range: *i.e.*, whether the response to a strong pulse feature is the **same** as to a weaker component. Another potential problem, a result of the dedispersion convolution, is the possible appearance of dips to either side of the pulse peaks. This problem is most prominent in the case of 1-bit sampling, but similar problem may easily occur in 2-bit quantized profiles. We have determined that the linearity is optimized by correctly choosing the spacing of the quantization levels or decision thresholds relative to the root-mean-square (rms) voltage of the incoming signal.

Consider the case of 2-bit quantization, with decision thresholds  $-V_{ref}$ , 0 and  $+V_{ref}$  and the decoded output levels spaced to be  $-n$ ,  $-1$ ,  $1$  and  $+n$ , where  $n$  is not necessarily an integer. We have found, using simulations, that  $|V_{ref}| \sim 1.0V_{rms}$  and  $n \approx 3.8$  are optimal values for these parameters, as compared to using  $|V_{ref}| = 1.0$  and  $n = 3$  (Thompson, Moran, Swenson, 1986). In our simulations, we start with generating a series of Gaussian random numbers (RN) with a mean zero and standard deviation of 1. We digitize the random numbers, sample-by-sample, with particular symmetric thresholds ( $\pm V_{ref}$ ). The digitized value was assigned a weight (D) of  $+LOW$  or  $+HIGH$  if the random number was smaller than  $+V_{ref}$  or larger respectively. Similarly, a weight of  $-LOW$  or  $-HIGH$  was assigned if the value was higher than  $-V_{ref}$  or lower respectively. For various values of  $V_{ref}$ ,  $LOW$  and  $HIGH$ , we compute a simple chi-square quantity, which **measures** the departure of the digitized numbers from analog numbers, which was defined by  $\sum_{i=1}^N (D_i - RN_i)^2 / N$ . We now track this value of chi-square as a function of  $V_{ref}$ ,  $LOW$  and  $HIGH$ . For a more faithful reconstruction, this value would be, minimized. The results, even though obtained with random numbers as input, are valid for our data since pulsar signals are weak in the decameter band.

Stairs (1998) has dealt with this issue in detail, and our values match with her optimum parameters well. It was shown, that setting  $|V_{ref}| = 1.4V_{rms}$  and  $n = 4$  best preserves the pulse shape while making the final signal-to-noise ratio roughly 0.82 of the analog value, as compared to the 0.66 fraction expected from using  $|V_{ref}| = 1.0$  and  $n = 3$  (Thompson, Moran, Swenson, 1986).

In practice, on-source response of **GEETEE** is modulated by beam-flips over timescales of  $40 \text{ sec}(\delta)$ s (section 2.1.2) and there are systematic changes in the system gain of the order of 2dB. A dynamic setting with  $|V_{ref}| = 1.4V_{rms}$  was not possible. Therefore, we estimated the quantized  $V_{rms}$  at the beginning of the data acquisition by computing histograms of the incoming data using  $n = 3$ . We then adjusted the input attenuation until the  $|V_{ref}|$  is about  $V_{rms}$ . This arrangement made it possible for the digitization thresholds to remain close to the optimum value in entire acquisition.

### 2.3.3 An Effective Spectrometer

The raw spectrum, with a desired number of channels ( $n_{chan}$ ), is computed from the digitized voltage samples in overlapping blocks of  $2n_{chan}$  by means of Fourier Transforms. The maximum time resolution in each channel then is the inverse of the channel width. If so desired, the output is obtained by adding a specified number of consecutive spectra ( $m$ ) together. In this case the time resolution is  $(m n_{chan})^{-1}$  s.

This way, we construct the output of an effective spectrometer output with  $n_{chan}$  spectral channels, as a function of time, with the desired time resolution (referred as  $\tau_{\Delta\nu}$ ).

#### Optimum resolution consideration

We now have a data matrix of  $n_{chan}$  channels with a desired time resolution ( $\tau_{\Delta\nu}$ ). If we know the amount of dispersion caused by the interstellar medium, we can correct the differential dispersion delay within our band relative to some reference channel (section 1.3.1). Due to this procedure, any dispersion delay spread within a single channel remains, however, uncompensated and thus effects another time constant ( $\tau_d$ ). Other contribution to the temporal smearing arise due to the interstellar scattering ( $\tau_{sc}$ ). The effective time resolution can, therefore, be written as,

$$\tau = \sqrt{(\tau_{\Delta\nu})^2 + \tau_d^2 + \tau_{sc}^2} \quad (2.1)$$

where,  $\tau_d = 8300 DM \Delta\nu / n_{chan} v^3$  s,  $\tau_{\Delta\nu} \simeq (n_{chan} 10^{-6} / \nu)$  s and  $\Delta\nu$  &  $\nu$  are bandwidth & central frequency of observation (in units of MHz) respectively.

We choose  $n_{chan}$  so that  $\tau_d = \tau_{\Delta\nu}$ , for an optimum smoothing (Deshpande, 1989). This condition leads us to an optimum number of channels for dedispersion in the present case as

$$n_{chan}^{opt} \sim 440 (DM)^{1/2}. \quad (2.2)$$

#### Interference detection and excision

Shown in figures 2.4 and 2.5 are the raw time-series data and the raw spectra, where dispersion correction has *not* been applied. Such plots give information on the quality of the data and the presence of any interference which is necessarily "local" (so, undispersed).

The raw time series essentially shows the variations of the system gain with time. The jumps in the power level, most notably close to 135 and 205 seconds, are due to gain changes corresponding to beam-flips during source tracking (using discrete beam directions). The time duration between two successive beam-flips is  $40 \sec(\delta)$  seconds, where  $\delta$  is the source declination.

Any large fluctuations (say,  $> 10 \text{ rms}$ ) over a time-duration much shorter than the transit time across the beam-width of the array in the E-W, which corresponds to about **1.5** minutes at  $\delta = 0$ , are due to interference.

The interference is either narrow-band, in which case it is seen as sharp peaks in the spectrum (figure **2.5**). Such an interference consists of broader spike-like recurring variations over a longer duration in the time-domain, and may occur due to terrestrial radio-broadcast signals. Sharp peaks in the time domain, typically due to electric lightning or due to faulty electric gadgets in the near vicinity of the antenna, on the other hand, have a much broader spread in the raw frequency spectrum.

Different kinds of interference were treated after visual inspection of the raw time series and its radio-frequency spectrum. Narrow- and broad-band interference are apparent in the spectra as large changes in a channel power relative to the neighboring channels. Channels with fluctuations typically more than **5** times of fluctuations in the nearby channels were 'flagged' for rejection from the later analysis.

By summing the spectral contribution across the spectrum, after rejecting the flagged interference channels, we obtain a time sequence similar to the one shown in the figure **2.4**. We manually deleted parts of the time series containing sharp peaks (typically  $> 10 \text{ rms}$ ) or interference over a broader duration.

Information about the raw time sequence and the spectrum is stored in an additional data file, called the 'config' file, which is accessed in the further analysis. The steps of interference excision are flexible. In case a major portion of the data has a continuous patch of large interference, the spectrum is computed again from the raw data (going back one stage in the analysis procedure) excluding that part of the raw data. Further steps in the analysis now depend upon the intended study of the pulsar.

### **2.3.4 Channel-wise folded profiles**

With the knowledge of the spin period of the pulsar, we fold the time series in each channels at that period. Such folded pulse profiles can be viewed across our band. The pulse peak shows an expected dispersion delay across the band, as shown in the figure **2.6**. This matrix of data, intensity as a function of channel number and phase bin, can be utilized in various ways.

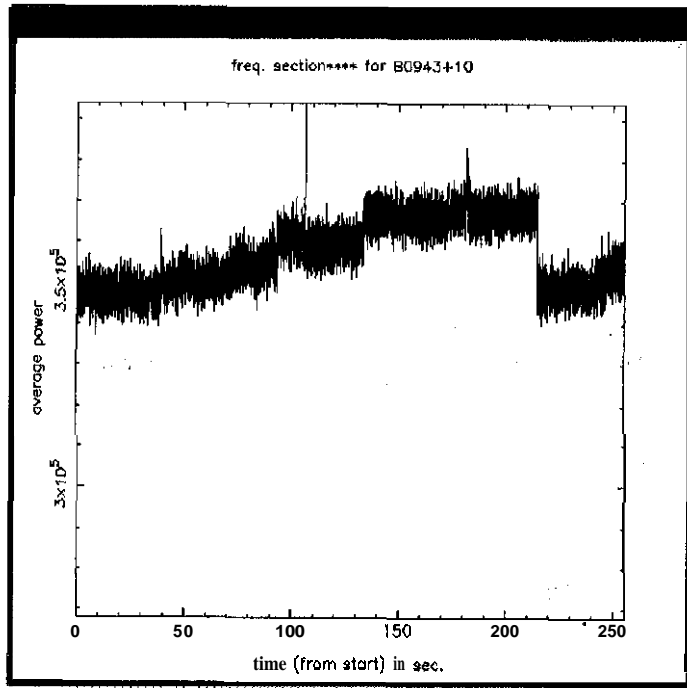


Figure 2.4: Raw intensity *vs* time sequence (corrected for slips): the power with a **1-MHz** band plotted is against time, where the time resolution was decided by the spectral resolution in the spectrometer equivalent output used. The power units are arbitrary, the time on the X-axis is in seconds (see text for details).

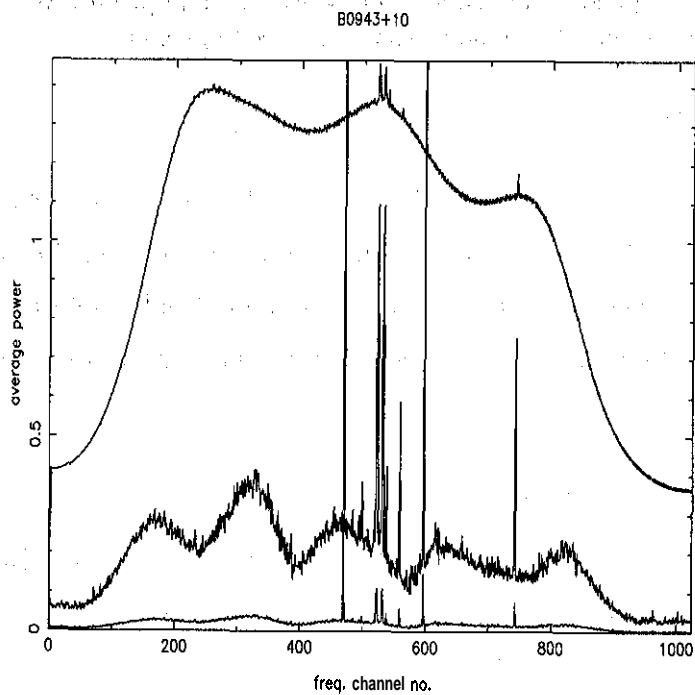


Figure 2.5: Radio-frequency spectrum obtained from raw data (corrected for slips). Shown is the average power plotted against the channel number (top curve): **1024** channels were used across this spectrum. The spectrum was normalized with respect to the peak value. The *rms* deviation estimated from the time variation of the channel power, around its average value, is shown by the bottom curve. For clarity, the same information is provided in the middle curve after multiplying it by a factor of 10.

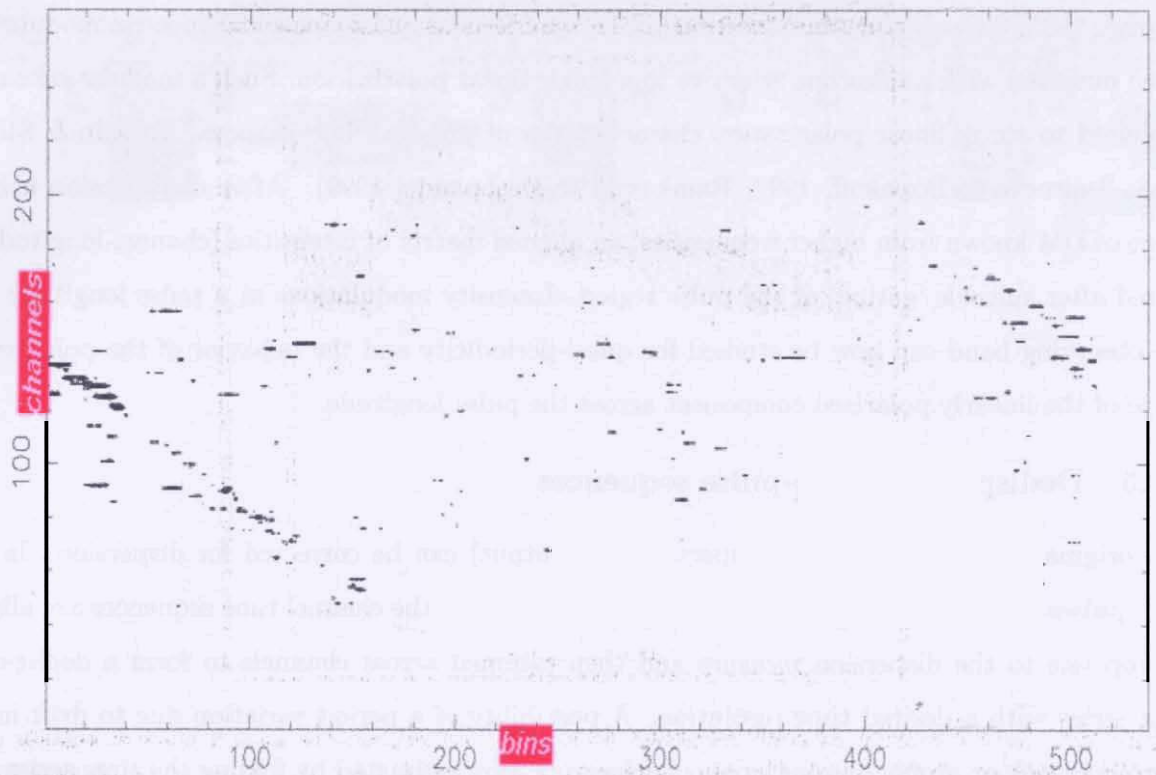


Figure 2.6: Dispersion of a pulse in the observed band of 1 MHz in the case of B1133+16. The folded pulse profile for individual channels are plotted for 256 channels (Y-axis), where the X-axis shows the number of the pulse bin (512 bins per period). The pulse peak gets folded back to the first bin when the dispersion delay is more than the pulsar period.

### Average, folded profile

We can now estimate the average profile of the pulsar from the above-mentioned **matrix of data**. Suitable delays **are applied to the** longitude-time series in each channel compensating **fix the dif-**ferential dispersion delay across the band. Folded pulse profiles from all the channels are summed ('channel-collapse') to obtain a dispersion-**U** & **—** (incoherent dedispersion, see **tion 1.3.1**)

### DM tuning and Faraday rotation

One can search for the DM of a pulsar. In order to do this, an assumed DM is varied in a desired range. For each assumed value of DM, an average profile is obtained by collapsing the channels. For certain phase delays across the band corresponding to the true DM, the S/N of the average pulse would peak. The error in this determination depends on the temporal and spectral resolutions available and the relative noise level.

Faraday rotation of the plane of polarization of broad-band signals, during propagation

through the intervening medium (section 1.3.1), manifests as quasi-sinusoidal spectral modulations when observed with a telescope sensitive to a single linear polarization. Such a modulation can be exploited to study linear polarization characteristics of pulsars (Suleymanova, Volodin & Shitov, 1988; Smirnova & Boriakoff, 1997; Ramkumar & Deshpande, 1999). After dedispersion using a value of DM known from higher frequencies, an **aligned** matrix of intensities (channel-longitude) is stored after suitable 'gating' of the pulse region. Intensity modulations at a pulse **longitude** over the observing band can now be studied for quasi-periodicity and the behavior of the **polarization** angle of the linearly polarized component across the pulse longitude.

### 2.3.5 Dedispersed single-pulse sequences

The original time-channel matrix (spectrometer output) can be corrected for dispersion. In this case, pulses from individual channels are not folded, instead the channel time sequences are aligned appropriate to the dispersion measure and then summed across channels to form a dedispersed time series with a desired time resolution. A **possibility** of a period variation due to drift in the sampling clock or profile binning exists. Such errors were estimated by folding the time series over a range of periods around its expected value and choosing the period for which the average profile had the best S/N.

At this stage, an output of individual pulses (after dedispersion), with suitable gating to select the regions of interest around the pulse peak, is available. Such pulse sequences can be used for the study of single-pulse fluctuations.

### 2.3.6 Flux calibration - standard point sources

Antenna gain can be calibrated from observations of celestial sources, whose flux densities at 35 MHz are known reliably, and are not variable. The power at the output of the antenna when the antenna is tracking an off-source region (OFF) and an on-source (ON) region are estimated. In this case, OFF corresponds to the system temperature  $T_{sys}$ , and ON corresponds to  $T_{sys} + T_A$ , where  $T_A$  is the increase in the system temperature due to the source. In this case, the gain, G, of the telescope can be written as,

$$G = \frac{(ON - OFF) \cdot T_{sys}}{OFF \cdot S_{35}} \quad (2.3)$$

The beam-flips during track mode are clearly visible, when the system gain changes by  $-5\%$ .

We observed 3C353 ( $S_{35} = 840$  Jy) as our calibrator source. In this mode of observations, we track the source over  $\sim 100$  sec and the average power on-source is computed. We also point the

telescope at blank field (away from the source), with the source a couple of degrees away in hour angle, and again record the data in tracking mode. The values of power off-source were computed.

The system temperature was obtained from the average background sky temperature using the available all-sky radio map at 34.5 MHz (Dwarakanath & Udayashankar, 1990). The average sky temperature, which dominates the receiver temperature in our system, is  $\sim 20,000$  K. The estimated values for power on-source and off-source are, 354406 and 285286, respectively, in arbitrary linear units. The flux density of 3C353 is 840 Jy (Dwarakanath, private communication). From eq. 2.3, the estimated gain of GEETEE is,

$$G_{estimated} = 5.5 K/Jy \quad (2.4)$$

The expected gain of the antenna is  $\sim 4K/Jy$ , and we find that our above estimate is affected by systematic errors in our measurement.

The general health of the antenna was monitored on a routine basis using a continuum receiver at GEETEE (section 2.1.2). Strong point sources (compared to the fan beam of our antenna), such as Cassiopeia A, Virgo A, were observed in transit mode. The system sensitivity was estimated and was found to be close to its expected value over our observation period.

# Chapter 3

## Average-Profile Studies of Pulsars

In Chapter 2, we described our observational set-up and analysis procedure. In this chapter, we present our results on average properties of pulsars using our data.

### 3.1 Pulse detections & average profiles

As mentioned earlier, we used only the East-West arm of the **GEETEE** for all our observations, which has a fan beam of  $0.5'' \times 25^\circ$  with its narrow width in hour angle. We carefully chose a sample of pulsars to be observed for our present study from the population of known pulsars. We describe our selection criteria for choosing our pulsar sample.

#### 3.1.1 Pulsar sample

We based our selection on the catalog of known pulsars (Taylor, Manchester & Lyne, 1993), wherein the properties of pulsars known from meter-wavelength observations were available. A subset of this population, expected to be detectable with a signal level of **50** or higher at **34.5 MHz**, were chosen for our observations.

The declination coverage was restricted to a range of  $-40''$  to  $+74''$ . This is due to the limited steerability of the **GEETEE**. The gain of the antenna reduces away from the local zenith, which is also accounted for in our assessment.

The minimum average flux density of a pulsar required for it to be detected with a signal-to-noise ratio of @ is given by,

$$S_{min} = \frac{\beta}{G} \frac{T_{rec} + T_{sky}}{\sqrt{\Delta\nu \cdot \tau \cdot N_{pol}}} \sqrt{\frac{W}{P - W}} \quad (3.1)$$

where,  $G$  is the gain of the antenna,  $T_{rec}$  and  $T_{sky}$  are the receiver and sky temperatures,  $\Delta\nu$  is the observational bandwidth in Hz,  $\tau$  is the integration time in seconds,  $N_{pol}$  is the number of polarizations used, and  $W$  &  $P$  are the pulse width and rotation period of the pulsar, respectively.



## Sky noise contribution

At decameter wavelengths, the sky background dominates over the receiver noise temperature.  $T_{sky}$  ranges between of 5000-40000 K (as compared to  $T_{rec} \sim 500$  K), and its average value is  $\sim 10,000$  K (Dwarakanath & Udayashankar, 1990). To account for the beam dilution effect due to our wide beam, we express the system temperature (neglecting the small contribution from the receiver noise) as,

$$T_{sys} = 5000 + \frac{T_{bg} \left( \frac{34.5}{408} \right)^{-2.55} - 5000}{7} \quad (3.2)$$

where,  $T_{bg}$  is the sky background temperature measured (and available from the catalog) towards direction of the pulsar at 408 MHz. The extrapolation to decameter band uses a spectral index of -2.55 (Dwarakanath, 1989).

## Estimation of pulsar **flux** at 34.5 MHz

We now estimate the expected pulsar flux densities in our band using the **available** properties at meter wavelengths. The available catalog tabulates the pulsar flux densities at one or more of the three values of frequency, 408 MHz, 600 MHz, and 1420 MHz. Using two of these values we estimate the spectral index of pulsar flux. In cases where this was not possible, due to non-availability of flux measurements at multiple frequencies, we assumed a spectral index of -1.6. Using the value of the spectral index, we determined the flux density at 100 MHz. We further assumed that all the pulsars display a turn-over in their radio spectra at  $\sim 100$  MHz, and the pulsar flux drops in decameter band with the same spectral index (with an opposite absolute sign) as displayed above 100 MHz. We estimate the expected flux density at 34.5 MHz using the expected flux at 100 MHz. In some cases, it was possible to refer to spectral measurements available down to 20-30 MHz (Malofeev et al., 1994) and assess the reliability of our estimation procedure.

## Pulse **width**

Possible pulse broadening effects were estimated using the model of galactic electron-distribution (Taylor & Cordes, 1993). We also estimated the pulse broadening due to RFM (section 1.1.3), by extrapolating pulsar pulse-widths measured at 400, 600, or 1400 MHz and assuming a radio frequency dependence of the pulse width to be  $\nu^{-0.25}$ . We have also ignored the effect of scatter broadening at those high frequencies.

Using eq. 3.1, we selected pulsars with an estimated peak pulse signal at 5 times or higher than the expected noise level. The sample contained a total of  $\sim 40$  pulsars. Pulsar **B0943+10** was

included in this list, though it was not selected by our criterion.

### 3.1.2 Average profiles

The selected sample was monitored in the summer of **1997**, when observations in the direction of every pulsar in the list were made for an effective duration of **-20** minutes. Some of the strong pulsars were observed again in **1999**. The acquired data were **analysed** for possible detections, and a total of **8** pulsars were detected from these data. In Figures **3.1** and **3.2**, we present average-pulse profiles corresponding to the detections using one single observation of each. Table **3.1** presents the relevant inferred parameters associated with the average profiles observed.

Average profiles at **34.5 MHz** show **an** increase in the pulse-width, and peak separation of the components in the case of 'double' profiles, when compared to the higher frequency results. The profile widths are known to increase at lower frequencies with a power-law index. Comparing with the higher frequency results of Slee *et al.*, **1987**, we find the index to be  $\gtrsim -0.3$ . We fitted our average profiles in terms of one or more Gaussian components. Based on these **fits**, we quote the values of the pulse widths and component separations.

**B0943+10** Figure **3.1** (a) shows a high resolution profile obtained from one observation of this pulsar on **13<sup>th</sup> Feb, 1999**. This pulsar is one of the rare cases where the flux density does not show any turnover even in the decameter band. These, and earlier **observations** by Deshpande & Radhakrishnan, **1992** and **1994**, (hereafter **DR92** and **DR94**, respectively) show that only one of the two average profile modes, observed and reported by Suleymanova *et al.*, **1998** *viz.* the 'B'-mode is most prominent in our observations. The separation of the two components (between their peaks) has increased to **58 ms** (the half power width of the profile being **86 ms**) from **31 ms** at **102 MHz**. This suggests that the separation is proportional to  $\nu^{-0.4}$ . We note that at meter wavelengths this pulsar displays a 'conal single' ( $S_d$ ) profile (Rankin, **1993**). The fact that this pulsar has been extremely difficult to detect above **400 MHz**, suggests that our sightline may be missing the emission beam in its entirety. The amplitudes of the two components are in the ratio of **1:1.9**, **whereas** their location from the fiducial point, defined as the point at which the pulsed power drops to the noise level, has a ratio  **$9.8 \pm 0.1 : 9.2 \pm 0.1$** .

**B0834+06** The **pulse** profile in this case is clearly resolved, and is shown in figure **3.1** (b). The observed pulse component separation is **25 ms**. The profile is narrower at higher radio frequencies, and a comparison with the **80-MHz** observations shows that the evolution is  $\nu^{-0.5}$ . When the profile is fitted with **2** Gaussian components, their widths turn out to be equal within the errors. The component amplitudes are in the ratio **1:0.9**.

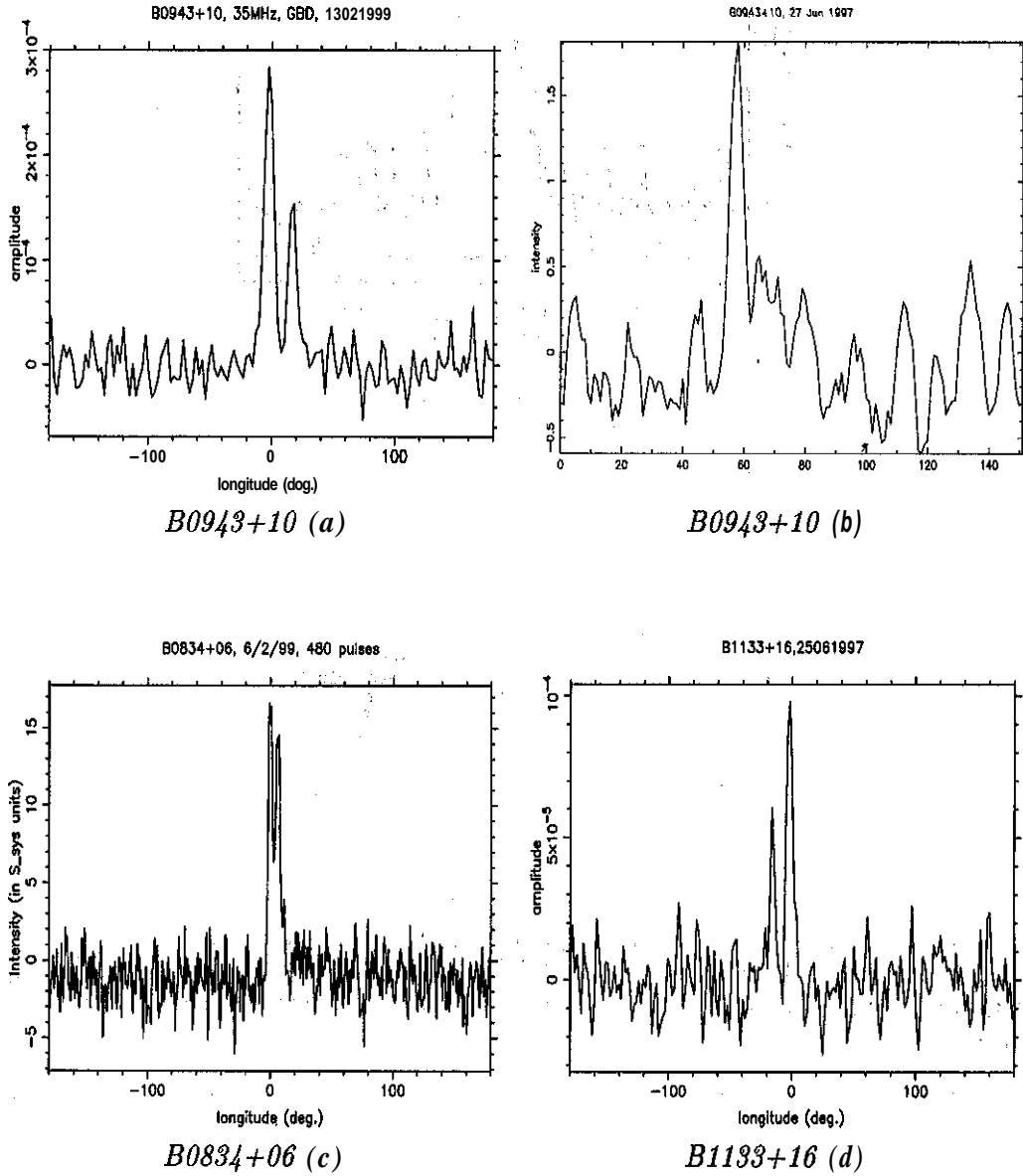


Figure 3.1: Average profiles of pulsars at 34.5 MHz. The intensities on Y-axis are in arbitrary units. The horizontal axis spans one pulsar period, *i.e.*  $360^\circ \equiv 1$  period.

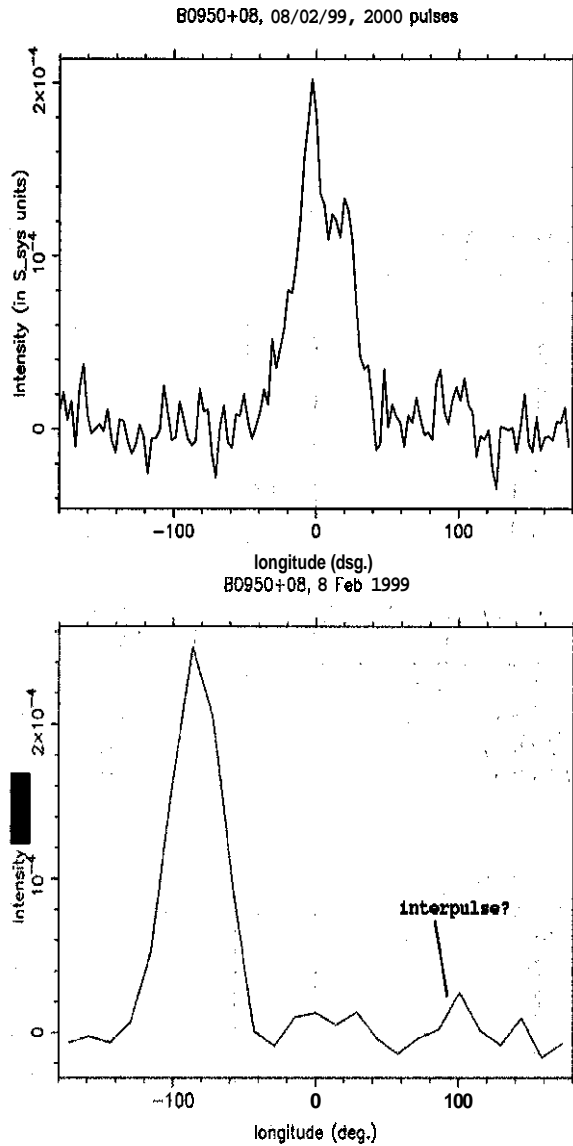


Figure 3.2: Average profiles of B0950+08 at 34.5 MHz, where intensities on the Y-axis are in arbitrary units. Some enhancement in intensity can be seen away from the main pulse in the bottom profile.

B1133+16 Figure 3.1 (d) shows the average-pulse profile of this pulsar, where the two components of the profile are well separated. The peak intensities of the two components are in the ratio  $0.6(\pm 0.03) : 1$ , in agreement with the estimation of DR92. We note that, in the frequency range 80 to 102 MHz, this intensity ratio is about unity (Slee et al., 1987, and Izvekova et al., 1979) and is greater than unity at 400 MHz (Manchester, 1971). At meter wavelengths, the leading component dominates over the other, unlike our profile. The locations of the two components from the middle point are in the ratio 7.2:6.5, with an error bar of  $\sim 0.1$  on each value. A comparison with the profiles of Slee et al., 1987, yields a spectral index of  $\sim -0.3$  for the profile evolution.

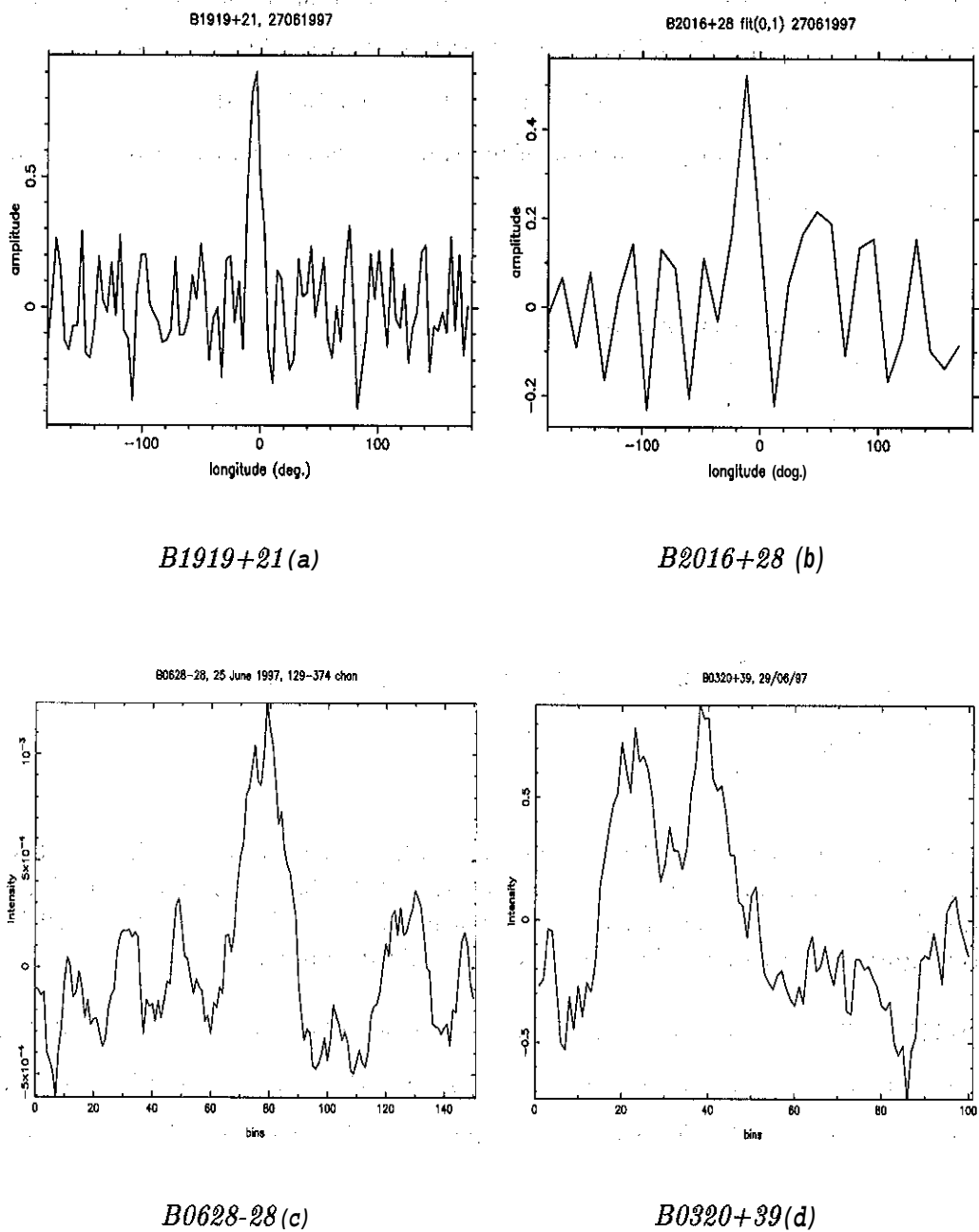


Figure 3.3: Average profiles of pulsars at 34.5 MHz. The intensities on the Y-axis are in arbitrary units, and the X-axis spans one rotation period of the pulsar.

**B0950+08** has the shortest period of the stars in our sample, due to which we could accumulate a large number of pulses from a single observation (typically  $\sim 2000$  pulses). We barely resolve the two components apparent in the pulse profile displayed in figure 3.2. The main pulse is very wide ( $80^\circ$ ). When the profile is modeled as two Gaussian components, we find that the pulse components display a ratio in intensities of 1:1.2, and their widths a ratio of 1.6:1. The pulse width at half-maximum, compared to **80-MHz** by Slee et al., 1987, indicates the spectral index of evolution to be  $-0.5$ . There may be a hint of interpulse emission, which, if real, has an intensity  $\approx 10\%$  of the main pulse.

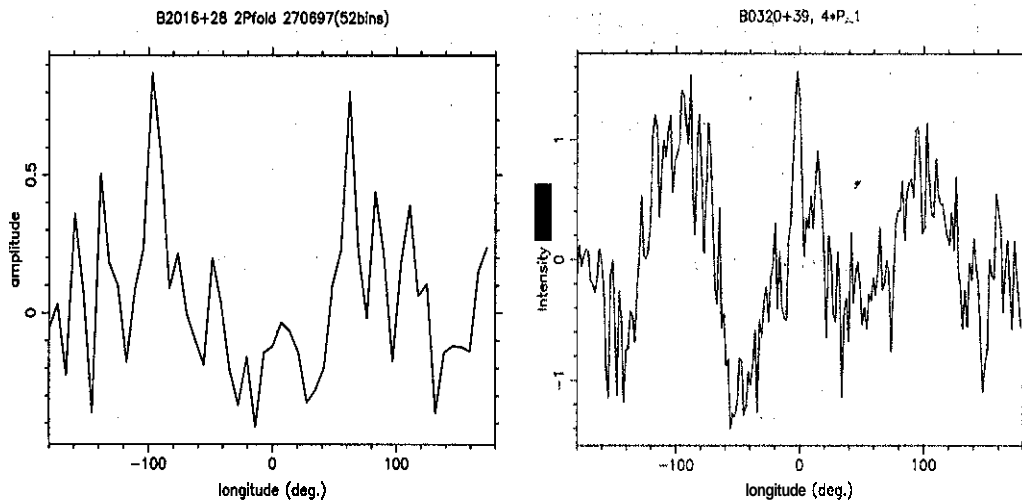


Figure 3.4: Confirming detection of two weak pulsars from our sample. **Left:** B2016+28, profile folded at twice the estimated pulse period. **Right:** B0320+39 profile folded at four times the estimated pulse period. Note that this pulsar is known to show periodic modulation with  $P_3 \simeq 4P_1$ . In both the figures intensities on the Y-axis are normalized to unity.

**B0628-28** This pulsar has the highest DM in our sample. We present its profile in figure 3.3. We suspect that this observation was affected by some interference. The profile consists of a single component and the observed pulse-width at half maximum is **120 ms**, consistent with DR94.

**B1919+21** The pulse profile, displayed in figure 3.3, has a single narrow profile. The width at half power is about **37 ms**. The width is smaller than the reported values at higher frequencies, and our results are consistent with those of DR94 & Slee, et al., 1987.

**2016+28 and B0320+39** Apart from the strong pulsars mentioned above, we could barely detect these two pulsars which are considerably weaker than others. The detection was confirmed by looking at profiles averaged over multiples of the true period, examples of which are presented in figure 3.4.

The profiles for all pulsars were obtained using 100-1000 pulses, each collected from single sequences.

### 3.1.3 Symmetry/Asymmetry aspects

The average profiles containing two components may display asymmetry in two aspects: the intensities of the two components may differ, and/or their locations around the central fiducial point, defined as the location where the pulsed power drops to the noise level in between the components, may be asymmetric.

As noted above, such asymmetries, with varying degree of significance, were observed in four cases of double profiles in our sample. Slightly non-circular polar caps, when sampled by symmetric trajectories of our sightline, will produce such asymmetries in the average pulse profile. Arendt & Eilek (2000) advocate such a scenario.

### 3.1.4 Profile, pulse-width evolution

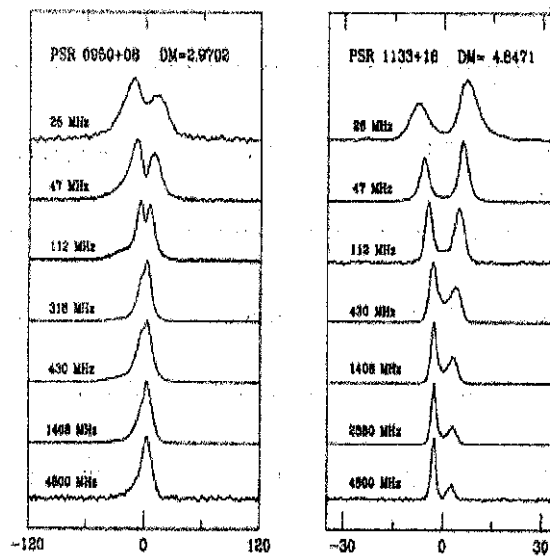


Figure 3.5: Time-aligned multi-frequency profiles of PSR0950+08 and PSR1133+16 (Phillips & Wolszczan, 1992)

All the pulsars display an increase in their pulse widths at lower radio frequencies, which can be fitted with a power law evolution with an index  $\gtrsim -0.4$ . We show such a behavior in the case of pulsars B0943+10 and B1133+16 in figure 3.5(a). This justifies our assumption made in section 3.1.1 about profile evolution of pulsars, while estimating the expected widths at 35 MHz.

Pulsar B1919+21 is a notable exception to this scheme of profile evolution, and RFM in general. We find the observed pulse to be narrower at decameter wavelengths. The pulse evolves

| Name     | period<br><i>s</i> | DM<br><i>pc/cm<sup>3</sup></i> | Integration<br>Time<br><i>s</i> | Average<br>Flux density<br>(35 MHz) <i>Jy</i> | Half power<br>pulse-width <sup>3</sup> <i>ms</i><br>(error <i>ms</i> ) | Component<br>separation <sup>3</sup> <i>ms</i><br>(error <i>ms</i> ) | Remarks <sup>4</sup> |
|----------|--------------------|--------------------------------|---------------------------------|---|--|--|----------------------|
| B0320+39 | 3.032              | 25.8                           | 540                             | $\sim 0.7^1$                                  | $\sim^2$   | $\sim^2$   | —                    |
| B0628-28 | 1.244              | 34.36                          | 572                             | 1   | 120 (5)  | -  | S                    |
| B0834+06 | 1.274              | 12.8579                        | 498                             | 0.5   | 36 (2.8)   | 25 (2.8)   | D                    |
| B0943+10 | 1.0977             | 15.35                          | 562                             | 2.4   | 86 (1.4)   | 58 (1.4)   | D                    |
| B0950+08 | 0.253              | 2.9701                         | 980                             | 0.8   | 33 (1.4)   | 16 (1.4)   | D, I                 |
| B1133+16 | 1.188              | 4.8471                         | 1212                            | 0.7   | 63 (1.4)   | 45 (1.4)   | D                    |
| B1919+21 | 1.337              | 12.4309                        | 523                             | 0.9   | 37 (6)   | -  | S                    |
| B2016+28 | 0.558              | 14.176                         | 321                             | $\sim 0.25^1$                                 | $\sim^2$   | $\sim^2$   | —                    |

Table 3.1: Relevant parameters of pulsars inferred from the average profiles of detection. <sup>1</sup> Estimated from the expected noise in the pulse. <sup>2</sup> Not available due to low signal-to-noise ratio. <sup>3</sup> Obtained from a Gaussian fit to the average profile, (the time-resolution of our data is  $\geq 0.98$  ms in all the cases). <sup>4</sup> S - **Conal** single, D - **Conal** double, I - a possible interpulse emission.



into a double profile in the decimeter band, where the pulse-width (and component separation) increases with radio frequency. Rankin (1983) interprets this behavior in terms of 'absorption features'. Rankin has pointed out several such known pulsars, which display a decrease in the pulse widths or separation of components in a certain frequency range, overlaying the secular increase in the pulse width with the increasing wavelength of observations. No known physical model anticipates any such 'absorption'. In the present case, however, the pulse narrowing at lower frequencies may be a result of "missing" one of the two components that are seen at higher frequencies.

The pulse profile of PSR B1509-58 is shown in Figure 1. The pulse width is approximately 1.5 ms at 100 MHz and increases to about 2.5 ms at 1.4 GHz. The pulse profile is double-peaked, with a main peak at approximately 0.5 ms and a secondary peak at approximately 1.5 ms. The pulse profile is shown for three different frequencies: 100 MHz (top), 1.4 GHz (middle), and 1.4 GHz (bottom). The pulse profile at 100 MHz is the most narrow, while the pulse profile at 1.4 GHz is the most wide. The pulse profile at 1.4 GHz shows a clear double-peaked structure, with a main peak at approximately 0.5 ms and a secondary peak at approximately 1.5 ms.

#### REFERENCES

- Rankin, J.M. (1983) *Astronomical Journal*, 88, 1000-1001.
- Rankin, J.M. (1984) *Astronomical Journal*, 89, 1000-1001.
- Rankin, J.M. (1985) *Astronomical Journal*, 90, 1000-1001.
- Rankin, J.M. (1986) *Astronomical Journal*, 91, 1000-1001.
- Rankin, J.M. (1987) *Astronomical Journal*, 92, 1000-1001.

## 3.2 Modulation index profiles

In a simple model, pulsar radio emission can be treated as an amplitude-modulated white noise. Average-pulse profiles, constructed for a pulsar from typically 1000 pulses, is a stable property of the pulsar-radio emission. The intensity fluctuations from pulse-to-pulse can be regarded as deviations caused by additional modulations over the the average-pulse profile. The observed deviations due to various phenomena can be classified into those intrinsic to pulsar phenomenon and to propagation effects of the intervening medium.

Various intrinsic modulations manifest at different time scales, which range from a micro-second to tens of seconds. Our time resolution allows us to study the modulations due to **subpulse** phenomena, which occur on millisecond time scales or higher. **Subpulse** fluctuations can be studied using fluctuation-spectral analysis, a topic discussed in detail in **the next** chapter. The spectrum of pulse modulations will have contributions due to fluctuations caused by scintillations in the path to the observer. As the scintillations caused by the interstellar medium **hâve** small decorrelation bandwidths compared to our observing band (1 MHz), they can be ignored in most of the cases.

Fluctuation spectra provide a lot of useful and detailed information on the frequency distribution of pulse modulations over **subpulse** scales. However, a quantity describing the average modulation strength can be estimated in a much simpler way. Such an information can be summarized in the form of a modulation index  $m$ , defined by

$$m = \frac{(\sigma_{ON}^2 - \sigma_{OFF}^2)^{1/2}}{\langle I \rangle}, \quad (3.3)$$

where  $\sigma_{ON}$  is the *rms* variation of the pulse intensities about the mean value  $\langle I \rangle$ , and  $\sigma_{OFF}$  is the *rms* value of the total system noise in the off-pulse region. Defined this way, we plot the index,  $m$ , at every pulse longitude to study the depth of modulation across the average profile.

We have computed the modulation-index profiles as a function of pulse longitude for seven pulsars. Such modulation-index profiles are presented in figures 3.6 and 3.7. Presented in this manner, the modulation indices display the presence of enhanced fluctuations, if any, at a given longitude location, when compared to other nearby longitude bins within the pulse, due to an underlying fluctuation associated with certain "intrinsic" phenomena.

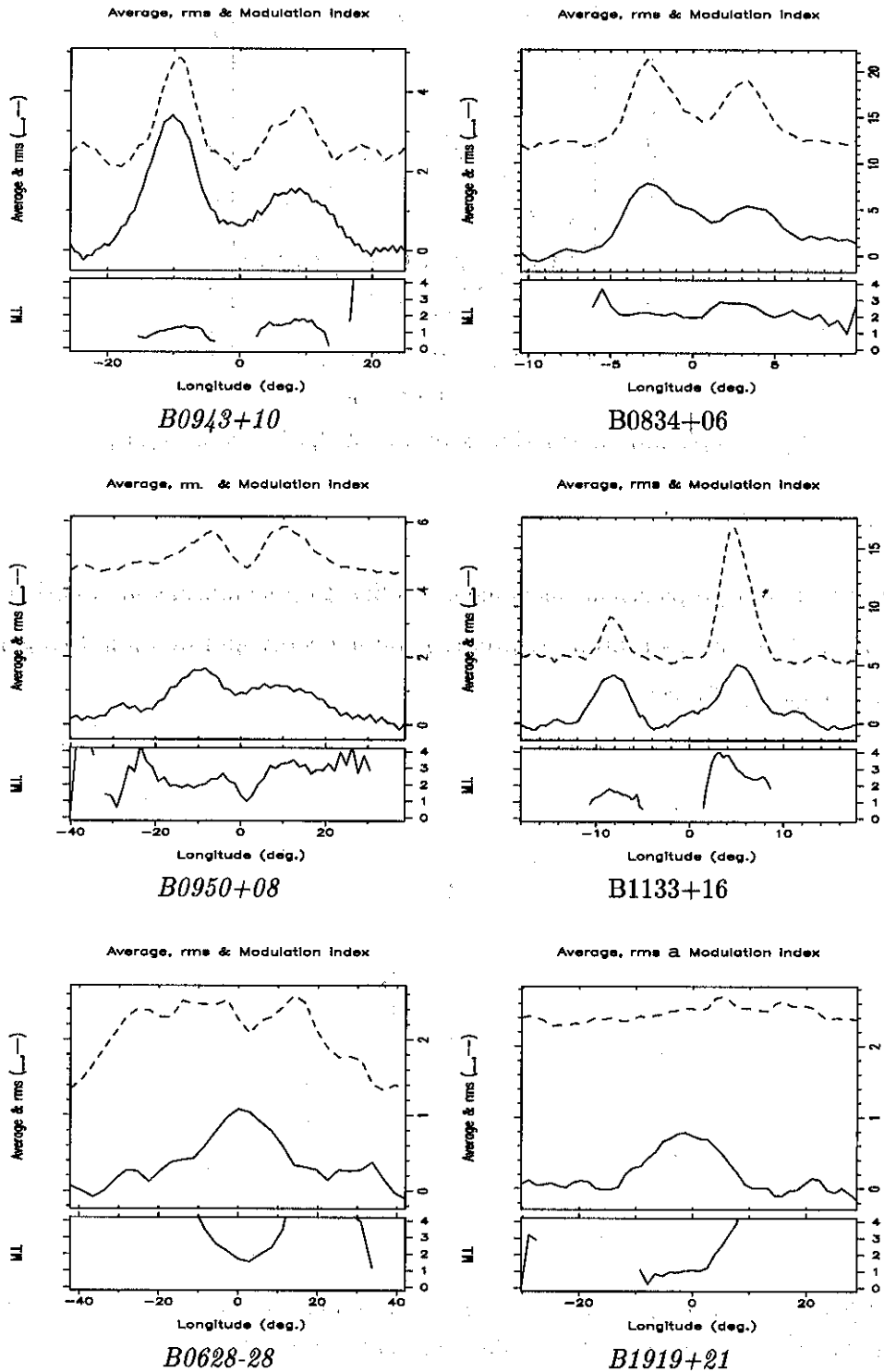


Figure 3.6: Modulation-index profiles of pulsars at 34.5 MHz. Shown in the top panel are the average intensity and its *rms* across the pulse longitude. The bottom panel shows the modulation index defined in eq. 3.3. It should be noted that the estimates of modulation indices are meaningful only where the average-pulse intensity is well above the noise floor.

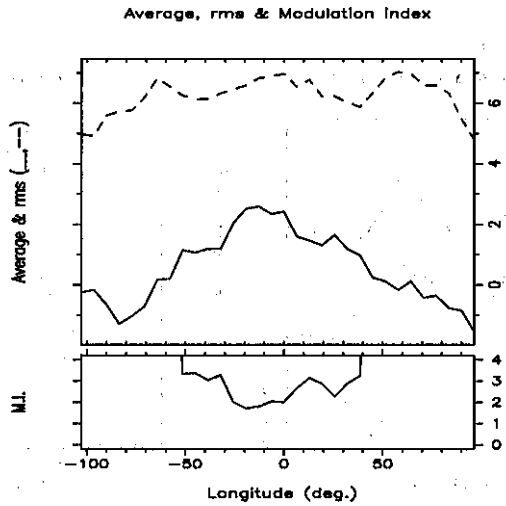


Figure 3.7: Modulation-index profile of B2016+28 at 34.5 MHz

### 3.3 Flux estimates

There are intrinsic and propagation phenomena leading to a significant modulation of the pulse signal. The task of measuring a properly averaged pulse energy and its radio-frequency spectrum is, therefore, not straightforward.

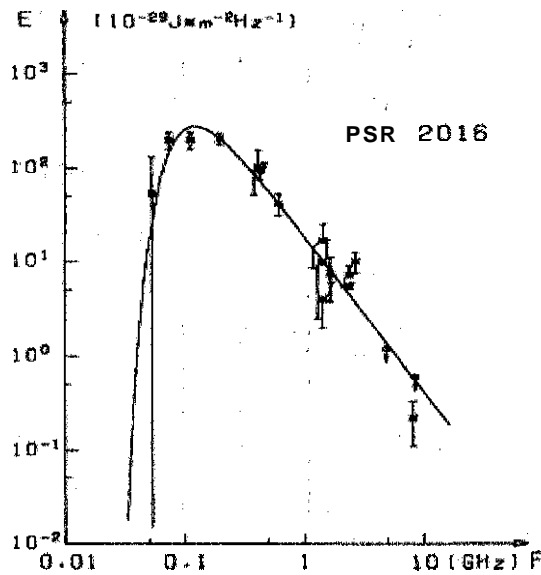


Figure 3.8: Flux density spectrum of B2016+28. The frequencies on X-axis are in GHz, while the average-flux densities on Y-axis are in the units of mJy (Sieber, 1973)

Radio flux-density spectra of many pulsars have been investigated based on the reported flux measurements at various radio frequencies (Malofeev et al., 1994). A typical example of such a spectrum is shown in figure 3.8. Typically, pulsar flux densities show a decrease with increasing frequencies and follow a steep power law,  $S_\nu \propto \nu^{-\alpha}$ , compared to the behavior seen for other

non-thermal sources. The spectral index ( $\alpha$ ) falls between -1 and -3 at decimeter wavelengths. The average pulse energy displays a turnover typically close to 100 MHz, below which the flux density displays more or less a flat spectrum or even a decline. The reasons for such a turnover are believed to be intrinsic to the pulsar, except for some short-period, distant objects, where it is attributed to the reduction in the pulse intensity due to scatter-broadening in the interstellar medium (*e.g.* the Vela pulsar).

In table 3.1, we have presented the flux density estimates from our observations. These values were obtained by fitting Gaussian profiles to the pulsar profiles. The off-pulse noise was equated to the estimated noise in the average-pulse profile and the average-flux density was estimated from the total area under the pulse. Our measurements are consistent with the published spectra, see Malofeev *et al.*, 1994, for comparison.

### 3.3.1 Variability

Estimates of flux density, are prone to errors due to source variability, apart from calibration errors. We discuss below two specific cases, *viz.*, the scintillation effects, and the intrinsic modulations.

#### Scintillation effects

Pulsars, as seen by a distant observer, are practically point sources. The propagation of the pulsed signal through the plasma irregularities leads to scattering of radio waves. This manifests into radio scintillation, similar to the observed twinkling of stars, viewed in the observer's plane. In a simple model, one considers a thin slab of scattering electron-density inhomogeneities along the line of sight and the resultant random refractive index of the medium as seen by the wave in slightly different directions (Scheuer, 1968). The interference of the different parts of the corrugated wavefront leads to well developed amplitude scintillations, when viewed at a sufficient distance from the screen in the presence of a relative motion of the screen with respect to the line-of-sight. These scintillations have correlation timescales of a few tens of minutes, and have narrow correlation bandwidths ( $\lesssim 1$  KHz). These patterns sweep across the telescope location, and their associated variations in apparent intensity must be averaged over the correlation scales to produce correct estimates of "average" fluxes.

Scintillations may also be apparent when viewed over longer durations of a few days, which are related to refractive fluctuations in the interstellar medium on length scales of  $\sim 10^{12} - 10^{14}$  m and relative motions of the source and the observer on the Earth (Rickett, Coles & Bourgois, 1984).

Since our profiles were constructed from short data sequences, the inferred flux densities

have more uncertainty due to refractive "slow" scintillation. But, our bandwidth of 1 MHz is much larger than the decorrelation bandwidth of  $\lesssim 1\text{KHz}$  for diffractive scintillations. Hence, pulse-to-pulse variations or intra-pulse variations in our data (when significant) are most likely due to intrinsic variations.

### Intrinsic

Given that we average out the effect of diffractive scintillations, in the present case, the pulse energy variability over time-scales from one to many hundreds of pulse periods can safely be believed as being intrinsic, as long as local gain variations are calibrated for correctly. These slow variations are mostly related to subpulse modulations in pulsars, drifting and profile mode changes, *etc.*

One such case of B0950+08 is shown in figure 3.9, where the pulse energy appears variable over time-scales of about 100 seconds.

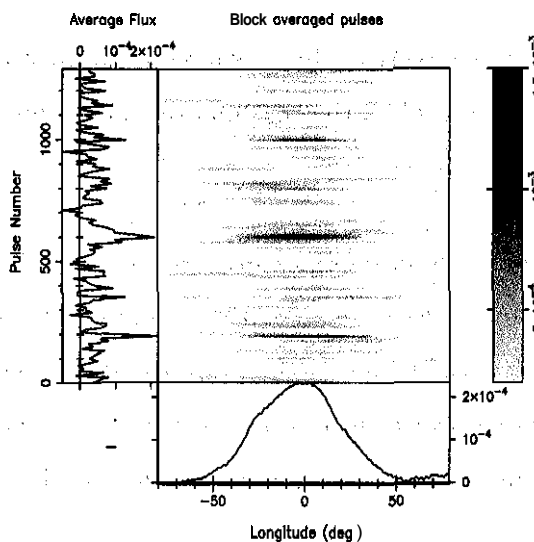


Figure 3.9: B0950+08: Variations of pulse energy at 35 MHz over a timescale of 100s of pulses.

### 3.4 Summary

In this chapter, we presented the average properties of 8 pulsars at 34.5 MHz using our observations with Gauribidanur array. We based our sample selection on the catalog of known pulsars (Taylor, Manchester, & Lyne, 1993), wherein the properties of pulsars known from the meter wavelength observations were available. We estimated the expected pulsar flux densities in our band for the candidates using their available properties at meter wavelengths and the short-list consisted of pulsars that could be detected with 1000 s integration. The sample contained a total of  $\sim 40$  pulsars. Pulsar B0943+10 was included in this list, though it was not selected by our criterion.

The selected sample was monitored in the summer of 1997, when observations in the direction of every pulsar in the list were made for an effective duration of  $\sim 20$  minutes. Some of the strong pulsars were observed again in 1999. The acquired data were analysed, and a total of 8 pulsars were detected. We have presented the average-pulse profiles obtained in these cases. The relevant inferred parameters associated with the average profiles observed are also presented.

Average profiles at 34.5 MHz show an increase in the pulse width, and component separation in the case of 'double' profiles, when compared to those at higher frequencies. The profile widths are known to increase at lower frequencies following a power law. Comparing with higher frequency results of Slee et al., 1987, we find the power law index to be steeper than  $\nu^{-0.3}$ . The average profiles containing two components may also display asymmetry in two aspects: the intensities of the two components may differ, and/or their locations around the central fiducial point, defined as the location where the pulsed power drops to noise level in between the components, may be asymmetric. Such asymmetries, with a varying degree of significance, were observed in four cases of double profiles in our sample. Such asymmetries can originate from a slight non-circularity of the polar cap being sampled by symmetric locus of our sightline, a scenario suggested by Arendt & Eilek (2000).

Our time resolution allows us to study the intrinsic modulations due to subpulse phenomena, which occur on milli second time scales or higher. Information about the strength of such modulations can be obtained by measuring modulation index  $m$  at every pulse longitude to study the depth of modulation across the pulse profile. We have computed the modulation index profiles as a function of pulse longitude for seven pulsars, and these results are presented. The modulation indices are seen to vary across longitude, and are, therefore, most likely due to an underlying "intrinsic" fluctuation phenomena.

Radio-flux density spectra of many pulsars have been studied based on the reported flux

measurements at various radio frequencies (Malofeev et al., 1994). Typically, pulsar flux densities show a decrease with increasing frequencies and follow a steep power law,  $S_\nu \propto \nu^{-\alpha}$  ( $-1 > \alpha > -3.0$ ), and display a turnover typically close to 100 MHz, below which flux densities have a more or less flat spectrum or even a decline. We have presented the flux-density estimates from our observations at 34.5 MHz. These estimates were obtained by fitting Gaussian profiles to the pulsar profiles. The area under the fitted profile was calibrated to get the average-pulse energy. Our measurements are consistent with the published spectra, based on earlier measurements.

Estimates of flux density are prone to errors due to source variability, apart from systematic calibration errors. We have discussed two specific cases, *viz.*, the scintillation effects and the intrinsic variability.

Scintillation effects are caused by the irregularities in the interstellar medium (ISM) along the line of sight. These irregularities cause the radio waves to be scattered, leading to a fluctuation in the received signal strength. This is particularly noticeable at higher frequencies. In our case, the pulsar signal at 34.5 MHz is relatively stable, but we have observed some small-scale variations in the pulse profile, which could be due to scintillation effects. The intrinsic variability of the pulsar is another source of error. Pulsars are known to exhibit changes in their pulse profiles over time, which can affect the flux density estimates. We have observed some changes in the pulse profile of the pulsar over the course of our observations, which could be due to intrinsic variability.

The flux density estimates presented in this paper are based on the assumption that the pulsar signal is a Gaussian pulse. This assumption is generally valid for most pulsars, but it may not be accurate for all pulsars. For example, some pulsars exhibit complex pulse profiles with multiple peaks and troughs, which could affect the flux density estimates.